# Robust Electrical Impedance Tomography for Respiratory Monitoring

Xiao-Peng Li, *Member, IEEE*, Zhang-Lei Shi, Meng Dai, Hing Cheung So, *Fellow, IEEE*,
Guangdong Xue, Zhanqi Zhao, and Lin Yang

***Abstract*—Thoracic electrical impedance tomography (EIT) is a crucial bedside monitoring tool, particularly valuable in pulmonary and critical care medicine. However, its routine clinical application is restricted in the presence of poorly contacting electrodes, patient movements, medical interventions, and nursing procedures. This is because these practical factors induce impulsive noise in EIT boundary voltages, severely degrading EIT imaging performance. In this article, to handle this issue, we devise a robust EIT (REIT) imaging method, which is able to promote the clinical application of thoracic EIT. We first reformulate the EIT boundary voltage change model, where the additive noise is separated into dense Gaussian and sparse outlier components. We then exploit $\ell_2$-norm and $\ell_0$-norm to formulate the optimization problem, in which the former and the latter are employed to resist the Gaussian noise and the impulsive noise, respectively. Subsequently, we adopt proximal alternating minimization (AM) and projected gradient descent (PGD) to tackle the resultant optimization task. Despite that the suggested method introduces an auxiliary parameter, we propose an adaptive strategy for its determination. Furthermore, we prove that the objective value sequence is convergent and the variable sequence converges to a critical point with at least a sublinear rate. Numerical simulation and phantom experiment exhibit that the devised approach reconstructs higher quality EIT images than the state-of-the-art (SOTA) algorithms when EIT boundary voltages comprise strong interference. Finally, we test the suggested algorithm on two patients data measured in real clinical environments to show its practical robustness.**

***Index Terms*—Electrical impedance tomography (EIT), impulsive noise, robust algorithm, sparse recovery.**

## I. Introduction

ELECTRICAL impedance tomography (EIT) is a medical imaging modality that attaches conducting surface electrodes to the skin around the body part. Subsequently, small alternating currents are applied to partial electrodes or all of the electrodes. In the meantime, current stimulations and surface voltages are integrated to visualize internal impedance distributions, that is, a tomographic image of a body part [1], [2], [3], [4]. The noninvasive nature and radiation-free characteristics make it an attractive real-time imaging tool that can be used at the patient's bedside [5], [6]. Its potential usefulness in clinical scenarios has gained considerable interest in the medical community. Specifically, it can be applied to monitor lung ventilation, track cryosurgery injury progress, facilitate early breast cancer detection, and monitor fetal movements [7], [8], [9], [10]. Among these applications, thoracic EIT is the most active and promising as it is able to optimize tidal volumes [11], assess lung recruitability [12], quantify the impact of recruitment maneuvers [13], analyze the effects of suctioning or rehabilitation [14], and evaluate regional lung function [15], [16]. In addition, thoracic EIT garners increasing acceptance for pulmonary and critical care medicine due to its unique capability to provide regional information on lung ventilation and perfusion [17].

As a soft-field imaging modality, thoracic EIT is an ill-conditioned and ill-posed mathematical inverse problem, making it highly sensitive to noise [18]. This sensitivity constitutes a significant barrier to the standardization of thoracic EIT as a medical tool as it is vulnerable to various clinical interferences [19]. In practice, the interferences arising from poorly contacting electrodes, patient movements, medical interventions, and nursing procedures induce severe fluctuations. The interference corrupts the respiratory EIT impedance signals, thereby posing challenges for the interpretation and evaluation of EIT data. For instance, a patient requires an examination to assess changes in lung ventilation follow-

---

Received 28 February 2025; revised 29 May 2025; accepted 16 June 2025. Date of publication 4 July 2025; date of current version 10 July 2025. This work was supported in part by the National Natural Science Foundation of China under Grant 62401373, Grant 62306337, Grant 52277235, and Grant 470088; in part by the Young Innovative Talents Project of Guangdong Provincial Department of Education (Natural Science), China, under Grant 2023KQNCX063; in part by the Joint Founding Project of Innovation Research Institution Xijing Hospital under Grant LHJJ24YG03; and in part by the 2035 Excellence Pursuit Plan Level B of Shenzhen University under Grant 2022B009. The Associate Editor coordinating the review process was Dr. Emanuele Piuzzi. *(Corresponding author: Lin Yang.)*

This work involved human subjects or animals in its research. Approval of all ethical and experimental procedures and protocols was granted by the Ethics Committees of the Air Force Medical University under Application No. KY20224101-1 and the Human Research Ethics Committee of the Tangdu Hospital of Air Force Medical University under Application No. K202212-13.

Xiao-Peng Li is with the State Key Laboratory of Radio Frequency Heterogeneous Integration, Shenzhen University, Shenzhen 518060, China (e-mail: x.p.li@szu.edu.cn).

Zhang-Lei Shi is with the College of Science, China University of Petroleum (East China), Qingdao 266580, China (e-mail: zlshi@upc.edu.cn).

Meng Dai is with the Department of Biomedical Engineering and Innovation Research Institution, Xijing Hospital, The Fourth Military Medical University, Xi'an 710032, China (e-mail: daimeng@fmmu.edu.cn).

Hing Cheung So is with the Department of Electrical Engineering, City University of Hong Kong, Hong Kong, SAR, China (e-mail: hcso@ee.cityu.edu.hk).

Guangdong Xue is with the School of Mathematics and Statistics, Donghua University, Shanghai 201620, China (e-mail: gdxue@dhu.edu.cn).

Zhanqi Zhao is with the School of Biomedical Engineering, Guangzhou Medical University, Guangzhou 511436, China, and also with the Department of Critical Care Medicine, Peking Union Medical College Hospital, Beijing 100005, China (e-mail: zhanqizhao@gzhmu.edu.cn).

Lin Yang is with the Department of Aerospace Medicine, The Fourth Military Medical University, Xi'an 710032, China (e-mail: yanglin.0601@163.com).

Digital Object Identifier 10.1109/TIM.2025.3584152

ing pulmonary parenchymal resection. Despite of employing minimally invasive techniques, patient movement attributable to postanesthesia incision pain results in impulsive noise in EIT boundary voltages, which obstructs the assessment of EIT-based ventilation indices [20]. In the context of EIT measurement, the impulsive noise refers to brief, sudden, and often large voltages with sharp, while it rapidly changes over a short period. Similarly, in clinical trials assessing patients with chronic obstructive pulmonary disease using EIT, the standard forced vital capacity (FVC) test, which requires forceful exhalation, causes significant chest movement. This movement disrupts electrode contact and introduces strong interference in EIT boundary voltages, leading to severe artifacts into the EIT images and consequently preventing accurate calculations of pulmonary function indices [21].

Although it is possible to collect data again when poor electrode contact or a sudden disconnection of an electrode is detected, this approach is impractical in most clinical scenarios. For example, when a patient requires saline injection to observe ventilation-perfusion dynamics, safety concerns make it inadvisable to administer hypertonic saline again within a short period. Similarly, for elderly patients with chronic obstructive pulmonary disease undergoing routine pulmonary function test combined with EIT monitoring, repeating FVC actions can exacerbate symptoms, such as dyspnea. In such cases, prioritizing patient safety, physicians are likely to terminate the pulmonary function test. Therefore, there is an urgent need to enhance the EIT robustness by mitigating the impact of strong interference on EIT images to facilitate clinical adoption. To this end, researchers have proposed several approaches, which can be classified into two categories, namely, methods to improve the quality of EIT boundary voltages and robust algorithms for EIT imaging in the presence of impulsive errors.

Under the assumption that all valid measurements are related by the image reconstruction model, while those from erroneous electrodes are unrelated, Asfaw and Adler [22] propose to automatically detect erroneous electrodes and then compensate for the erroneous electrode using a technique in [23]. To improve the performance of erroneous electrode detection, Hartinger et al. [24] utilize the principle of voltage-current reciprocity for real-time management of faulty electrodes, which enables EIT image reconstruction without the prior knowledge of electrode status. However, these algorithms encounter limitations when dealing with a large number of interfered electrodes. Besides, the discrete wavelet transform is exploited to compensate EIT measurements corrupted by common clinical motion artifacts [25], whereas its application is limited as it requires selecting an appropriate wavelet basis function for each patient. In recent, the deep learning techniques have been applied to compensate the invalid data when partial electrodes disconnect [26], [27], [28]. Although the deep learning-based approaches have shown good performance in phantom experiments, their limited generalization ability may restrict their clinical application.

On the other hand, the postprocessing approach to remove movement artifacts is proposed. Herzberg et al. [29] introduce a novel graph-based fully convolutional network to postprocess EIT image on irregular finite element (FE) meshes, while Ye et al. [30] suggest a multiscale 1-D residual convolutional network to remove chaotic noise and interference from the conductivity distribution data and retain the target feature data. Beyond these neural network-based solutions, Mason et al. [31] develop a noise-based correction (NBC) method for improving the quality of EIT images. They also test the performance of NBC in EIT reconstructions with different injection-protocols, perturbations, and noise.

Furthermore, the robust EIT (REIT) imaging methods have been proposed. Dai et al. [32] combine temporal sequence reconstruction with electrode movement compensation to improve image quality when several electrodes move. However, it is worth mentioning that this method cannot effectively restrain dramatic electrode interference. To counteract the strong interference, Borsic and Adler [33] propose substituting $\ell_2$-norm with $\ell_1$-norm to minimize the estimation error, yielding a rosbut EIT imaging method. This robust algorithm is able to attain good performance in low-intensity interference, while its imaging quality degrades in the presence of high-intensity noise.

This article aims at devising a robust imaging method for thoracic EIT in the presence of impulsive errors in EIT boundary voltages. To this end, we first formulate the additive noise as two components, namely, dense Gaussian and sparse outlier constituents. To characterize the sparsity, we employ the nonconvex and nondifferential $\ell_0$-norm, which is able to resist the impulsive errors. Besides, the Gaussian noise is restrained using $\ell_2$-norm. Therefore, the thoracic EIT imaging task is formulated as a sparse recovery problem consisting of $\ell_2$-norm and $\ell_0$-norm terms. To tackle the resultant problem, we adopt proximal alternating minimization (PAM) [34], [35] as the solver, resulting in an alternating optimization procedure. One subtask comprises three $\ell_2$-norm terms, and the other subproblem includes the $\ell_0$-norm regularization term. In particular, we exploit the projected gradient descent (PGD) method [36] to directly tackle the latter. Furthermore, theoretical properties of the suggested method, including computational complexity, as well as the convergence behaviors of the loss function value and variable sequence, are provided. Numerical simulation and phantom experiment demonstrate the superiority of our method over the conventional algorithms. Besides, we conduct patient experiments in real clinical environment to show the practical usefulness of the proposed algorithm. Our main contributions are summarized as follows.

1) *Novel Thoracic EIT Imaging Formulation:* We propose a novel thoracic EIT imaging method that is robust to impulsive errors in boundary voltages by formulating additive noise as a combination of dense Gaussian noise and sparse outliers.
2) *New Objective Function:* To handle the impulsive errors, we employ the nonconvex and nondifferentiable $\ell_0$-norm to characterize the sparse outlier component, combined with an $\ell_2$-norm to model the Gaussian noise, resulting in a nonconvex optimization problem for EIT imaging.
3) *Efficient Algorithm:* Despite that the proposed method is an iterative procedure, it is able to obtain the solu-

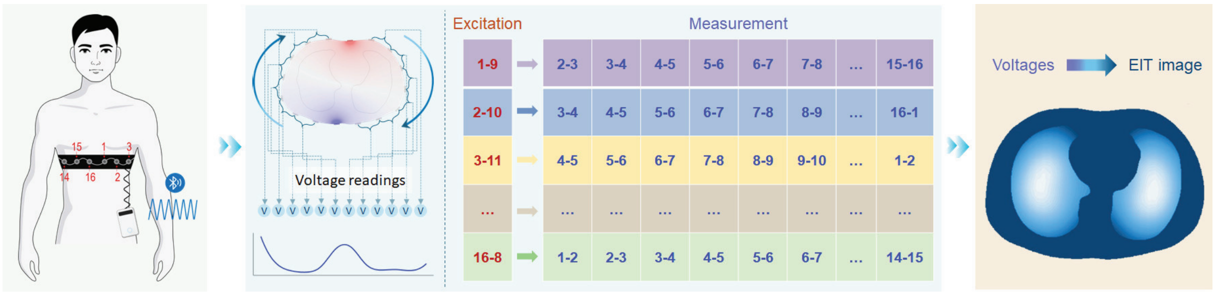

| Excitation | | Measurement | | | | | | | |
|---|---|---|---|---|---|---|---|---|---|
| 1-9 | → | 2-3 | 3-4 | 4-5 | 5-6 | 6-7 | 7-8 | ... | 15-16 |
| 2-10 | → | 3-4 | 4-5 | 5-6 | 6-7 | 7-8 | 8-9 | ... | 16-1 |
| 3-11 | → | 4-5 | 5-6 | 6-7 | 7-8 | 8-9 | 9-10 | ... | 1-2 |
| ... | → | ... | ... | ... | ... | ... | ... | ... | ... |
| 16-8 | → | 1-2 | 2-3 | 3-4 | 4-5 | 5-6 | 6-7 | ... | 14-15 |

Electrode attachment Data acquisition Image reconstruction

Fig. 1. Illustration of 16-electrode EIT system with the protocol of opposite-excitation and adjacent measurement.

tion in dozens of iterations. In addition, the suggested algorithm has the theoretical convergence guarantee, that is, the objective value sequence is convergent, while the variable sequence converges to a critical point with at least a sublinear rate.

4) *High-Quality Imaging:* Numerical results using synthetic, phantom, and patient data demonstrate that the devised method is superior to state-of-the-art (SOTA) approaches when thoracic EIT boundary voltages are corrupted by impulsive noise.

The remainder of this article is organized as follows. In Section II, we introduce notation and review the contemporary signal models. Problem formulation and the proposed algorithm are presented in Section III, where the convergence behavior and computational requirements of the proposed method are analyzed as well. In Section IV, numerical experiments are included to evaluate the devised method. Finally, concluding remarks are given in Section V.

## II. BACKGROUND

In this section, notation and signal model are presented, and relevant works are reviewed.

### A. Notation

Italics indicate scalars, bold lowercase letters represent vectors, and bold uppercase letters denote matrices. For a matrix $A \in \mathbb{R}^{M\times N}$, the $(i, j)$ entry is represented by $A_{i,j}$ or $a_{i,j}$. The $\ell_p$-norm with $0 < p \le 2$ of the vector is defined as $\|a\|_p = \left(\sum_{j=1}^{N} a_i^p\right)^{1/p}$, while the $\ell_0$-norm corresponds to the number of nonzero entries. The transpose operator is denoted as $(\cdot)^{\mathrm{T}}$, and the inverse operator is represented by $(\cdot)^{-1}$.

### B. Signal Model

In general, a thoracic EIT system, such as commercial Ventom-100, Medias Corporation, Suzhou, China, is equipped with 16 electrodes. If the system exploits the protocol of opposite excitation and adjacent measurement to collect data, one pair of opposite electrodes generates excitation, while the remaining 12 pairs of adjacent electrodes measure the resultant surface voltages. Then, the system switches the excitation pair until all pairs of opposite electrodes serve as excitation, which can be considered as a cycle. This procedure is depicted in Fig. 1. Therefore, EIT boundary voltage is obtained from $16 \times 12 = 192$ channels and thus can be represented as a vector $v_t \in \mathbb{R}^{192}$, where the subscript $t$ indicates the time index. Collecting $T$ instants, the EIT measurements can be represented as a matrix $V \in \mathbb{R}^{192\times T}$.

Before reconstructing an EIT image, the boundary voltage change should be calculated

$$\begin{aligned} \Delta v &= v_{t_2} - v_{t_1} \\ &= \Delta\tilde{v} + n \end{aligned} \tag{1}$$

where $\Delta\tilde{v} \in \mathbb{R}^{192}$ is the noise-free boundary voltage change, $n \in \mathbb{R}^{192}$ is the measurement noise vector, while $v_{t_2} \in \mathbb{R}^{192}$ and $v_{t_1} \in \mathbb{R}^{192}$ are the boundary voltages at $t_2$ and $t_1$, respectively.

Under the assumption that $n$ obeys Gaussian distribution, Grychtol et al. [37] propose exploiting $\Delta v$ to reconstruct the corresponding EIT image of conductivity change $\Delta\sigma$ between two time samples via the following optimization problem:

$$\min_{\Delta\sigma} \left\| \widetilde{W}(\Delta v - J\Delta\sigma) \right\|_2^2 + \lambda_1 \left\| \widetilde{Q}\Delta\sigma \right\|_2^2 \tag{2}$$

where $J \in \mathbb{R}^{192\times N}$ is the Jacobian (sensitivity) matrix of the forward map evaluated at an initial guess of the background conductivity, $\lambda_1 > 0$ is a penalty parameter, while $\widetilde{W} \in \mathbb{R}^{192\times 192}$ and $\widetilde{Q} \in \mathbb{R}^{N\times N}$ are defined as [37]

$$\widetilde{W}^{\mathrm{T}}\widetilde{W} = W = (\Sigma_n)^{-1} \tag{3a}$$

$$\widetilde{Q}^{\mathrm{T}}\widetilde{Q} = Q = (\Sigma_t)^{-1} \tag{3b}$$

where $\Sigma_n$ is the estimated noise covariance and $\Sigma_t$ is the effective covariance of the training targets, while $Q$ is the inverse of the effective covariance matrix. In general, $\Sigma_n$ is a scaled identity matrix $\sigma_n^2 I$, where $\sigma_n^2$ is the variance of noise. Since (2) is a linear least squares problem with an $\ell_2$-norm regularization term, we can attain its optimal solution via setting its gradient with respect to $\Delta\sigma$ to zero

$$2J^{\mathrm{T}}\widetilde{W}^{\mathrm{T}}\widetilde{W}J\Delta\sigma - 2J^{\mathrm{T}}\widetilde{W}^{\mathrm{T}}\widetilde{W}\Delta v + 2\lambda_1\widetilde{Q}^{\mathrm{T}}\widetilde{Q}\Delta\sigma = 0 \tag{4a}$$

$$\Rightarrow J^{\mathrm{T}}WJ\Delta\sigma - J^{\mathrm{T}}W\Delta v + \lambda_1 Q\Delta\sigma = 0 \tag{4b}$$

$$\Rightarrow \Delta\sigma^* = \left(J^{\mathrm{T}}WJ + \lambda_1 Q\right)^{-1} J^{\mathrm{T}}W\Delta v. \tag{4c}$$

However, the performance of (2) will be degraded when the EIT boundary voltages include impulsive noise that can be caused from patient movement, perspiration, manipulations by clinical staff, and defective electrode leads or electronics. The reason is that the $\ell_2$-norm amplifies the power of outliers, which is much larger than that of the Gaussian noise [38].

To resist outliers, Borsic and Adler [33] suggest exploiting $\ell_1$-norm to formulate the optimization problem, resulting in

$$\min_{\Delta\sigma} \|\widetilde{W}(\Delta v - J\Delta\sigma)\|_1 + \lambda_1\|\widetilde{Q}(\Delta\sigma - \Delta\sigma_0)\|_2^2 \tag{5}$$

where $\Delta\sigma_0$ is a prior model state. Then, the resultant task is handled using the primal-dual interior-point framework.

Compared with the $\ell_2$-norm, the $\ell_1$-norm weakens the impact of impulsive noise on the reconstructed EIT image, and thus, it is able to attain better imaging performance than $\ell_2$-norm in the presence of outliers. It should be noted that as the $\ell_1$-norm is an entrywise function, it considers that all channels of EIT boundary voltages $\Delta v$ contain impulsive noise [38], [39],whereas only a small partial of the channels is corrupted by outliers in practice. As a result, (5) is a bias model due to the adoption of the $\ell_1$-norm, leading to a suboptimal solution.

## III. ALGORITHM DEVELOPMENT

In this section, we present the devised method for thoracic EIT. We then analyze its convergence behavior and computational complexity.

### A. Proposed Model

First, we reformulate the boundary voltage change as

$$\begin{aligned}\Delta v &= \Delta\tilde{v} + n \\ &= \Delta\tilde{v} + g + o\end{aligned} \tag{6}$$

where $n$ is separated into dense Gaussian component $g \in \mathbb{R}^{192}$ and sparse outlier constituent $o \in \mathbb{R}^{192}$. Based on (6), we can employ two different norms to resist $g$ and $o$, respectively. The $\ell_2$-norm is the optimal selection to restrain the former [40], while the $\ell_0$-norm is the accurate measurement to characterize the latter [41]. Therefore, we formulate the thoracic EIT task as the following problem:

$$\min_{\Delta\sigma, o} \|\widetilde{W}(\Delta v - J\Delta\sigma - o)\|_2^2 + \lambda_1\|\widetilde{Q}\Delta\sigma\|_2^2 + \lambda_2\|o\|_0 \tag{7}$$

where $\lambda_2 > 0$ is a penalty parameter to control the sparsity of $o$. Compared to (2), the objective function of (7) has an additional regularization term for sparse outliers. With this term, the proposed optimization method has the capability to resist impulsive noise. In addition, we suggest a strategy to adaptively determine $\lambda_2$ for clinical application promotion in Section III-B.

### B. Proposed Algorithm

It is apparent that (7) is an unconstrained optimization problem with two variables, namely, $\Delta\sigma$ and $o$. Generally, alternating minimization (AM) [42] can be adopted as the solver, whereas it is difficult to guarantee the convergence of the variable sequence. To ensure the convergence, we exploit the proximal AM (PAM) [34], [35] to tackle (7), leading to the following alternating iterative procedure:

$$\begin{aligned}\Delta\sigma^{k+1} = \arg\min_{\Delta\sigma} &\left\|\widetilde{W}\left(\Delta v - J\Delta\sigma - o^k\right)\right\|_2^2 + \lambda_1\left\|\widetilde{Q}\Delta\sigma\right\|_2^2 \\ &+ \mu\left\|\Delta\sigma - \Delta\sigma^k\right\|_2^2\end{aligned} \tag{8a}$$

$$\begin{aligned}o^{k+1} = \arg\min_{o} &\left\|\widetilde{W}\left(\Delta v - J\Delta\sigma^{k+1} - o\right)\right\|_2^2 + \lambda_2\|o\|_0 \\ &+ \mu\left\|o - o^k\right\|_2^2\end{aligned} \tag{8b}$$

where $\mu > 0$ is a predefined proximal parameter and the last terms in (8a) and (8b) are called proximal regularizers. Note that $\mu$ can be set as a very small value as its role is to facilitate the convergence analysis. Next, we present the detailed procedure to handle (8a) and (8b), respectively. First, as (8a) is a linear least squares problem with two $\ell_2$-norm regularizers, we take its derivative with respect to $\Delta\sigma$, set the gradient to be zero, and then obtain its closed-form solution, given by

$$\Delta\sigma^{k+1} = \left(J^{\mathrm{T}}WJ + \lambda_1 Q + \mu I\right)^{-1}\left(J^{\mathrm{T}}W\left(\Delta v - o^k\right) + \mu\Delta\sigma^k\right). \tag{9}$$

Subsequently, we seek the solution to (8b). Prior to this, we analyze the structure of $\widetilde{W}$ to convert (8b) to a tractable problem. In (3a), as $W$ is a diagonal matrix, $\widetilde{W}$ is also a diagonal matrix and satisfies

$$\widetilde{w}_{i,i} = \sqrt{w_{i,i}}. \tag{10}$$

Therefore, (8b) is equivalent to the following scalar-form subproblems:

$$\begin{aligned}o_i^{k+1} = \arg\min_{o_i} &\left(\widetilde{w}_{i,i}\left(n_i^{k+1} - o_i\right)\right)^2 + \lambda_2|o_i| \\ &+ \mu\left(o_i - o_i^k\right)^2, i \in [1, 192]\end{aligned} \tag{11}$$

where $n_i^{k+1}$ is the $i$th entry of $n^{k+1} = \Delta v - J\Delta\sigma^{k+1}$. Then, for (11), an optimal solution can be obtained using the following method [43], [44]:

$$\begin{aligned}&o_i^{k+1} \\ &= \begin{cases}\dfrac{\widetilde{w}_{i,i}^2 n_i^{k+1} + \mu o_i^k}{\widetilde{w}_{i,i}^2 + \mu}, & \text{if } \frac{\lambda_2}{\widetilde{w}_{i,i}^2} \leq \left(n_i^{k+1}\right)^2 + \frac{\mu o_i^k}{\widetilde{w}_{i,i}^2} - \frac{\mu\left(o_i^k - n_i^{k+1}\right)^2}{\widetilde{w}_{i,i}^2 + \mu} \\ 0, & \text{otherwise.}\end{cases}\end{aligned} \tag{12}$$

From (12), it is known that the solution to (8b) is affected by $\lambda_2$. Consequently, we provide a strategy to adaptively determine it before updating (8b). To facilitate the analysis of $\lambda_2$, we set the proximal parameter $\mu$ to be 0, resulting in

$$o_i^{k+1} = \begin{cases} n_i^{k+1}, & \text{if } \sqrt{\frac{\lambda_2}{\widetilde{w}_{i,i}^2}} \leq \left|\left(n_i^{k+1}\right)\right| \\ 0, & \text{otherwise.}\end{cases} \tag{13}$$

If $n^{k+1}$ is considered as the fitting error with zero mean, $-(\lambda_2/\widetilde{w}_{i,i}^2)^{1/2} < n_i^{k+1} < (\lambda_2/\widetilde{w}_{i,i}^2)^{1/2}$ is considered as a confidence interval to identify outliers, namely, $n_i^{k+1}$ with $\sqrt{\lambda_2/\widetilde{w}_{i,i}^2} \leq |(n_i^{k+1})|$. To obtain a robust confidence interval in the presence of outliers, we suggest adopting the normalized median absolute deviation [45], [46] to calculate the standard deviation

$$\sigma_n = 1.4826 \times \mathrm{Med}\left(\left|n^{k+1} - \mathrm{Med}\left(n^{k+1}\right)\right|\right) \tag{14}$$

where Med$(\cdot)$ is the sample median operator. As a rule of thumb, the normalized median absolute deviation is not influenced very much by the presence of large outliers and thus provides a good robust alternative to the sample standard deviation [47].

**Algorithm 1** REIT

```
Input: $\Delta v \in \mathbb{R}^{192}$, $J \in \mathbb{R}^{192\times N}$, $\eta = 3$, $\lambda_1 = 10^{-2}$, $\mu = 10^{-8}$,
    and $K_{\max} = 50$
    for $k = 1, 2, \ldots, K_{\max}$ do
        1) Update $\Delta\sigma^k$ using the following procedure:
        $\Delta\boldsymbol{\sigma}^{k+1} = \left(\boldsymbol{J}^{\mathrm{T}}\boldsymbol{W}\boldsymbol{J} + \lambda_1\boldsymbol{Q} + \mu\boldsymbol{I}\right)^{-1}$
        $\left(\boldsymbol{J}^{\mathrm{T}}\boldsymbol{W}\left(\Delta\boldsymbol{v} - \boldsymbol{o}^k\right) + \mu\Delta\boldsymbol{\sigma}^k\right)$.
        2) Update $o^k$ using the following procedure:
        2.1) $n^{k+1} = \Delta v - J\Delta\sigma^{k+1}$
        2.2) $\sigma_n = 1.4826 \times \mathrm{Med}(|n^{k+1} - \mathrm{Med}(n^{k+1})|)$
        2.3) $\tau = (n^{k+1}) \odot (n^{k+1}) + \mu o^k./\mathrm{diag}\widetilde{W} \odot \widetilde{W}) - \mu^2(o^k - n^{k+1}) \odot (o^k - n^{k+1})/\mathrm{diag}(\widetilde{W}^2) + \mu$
        2.4) $o_i^{k+1} = \begin{cases} \dfrac{\widetilde{w}_{i,i}^2 n_i^{k+1} + \mu o_i^k}{\widetilde{w}_{i,i}^2 + \mu}, & \text{if } \eta\sigma_n \le \tau_i, \\ 0, & \text{otherwise.} \end{cases}$
    end for
Output: $\Delta\sigma^*$
```

Then, $\lambda_2$ is updated via

$$\sqrt{\frac{\lambda_2}{\widetilde{w}_{i,i}^2}} = \eta \times \sigma_n \tag{15a}$$

$$\Rightarrow \lambda_2 = \left(\eta \times \sigma_n \times \widetilde{w}_{i,i}\right)^2 \tag{15b}$$

where $\eta > 0$ controls the range of confidence interval.

The proposed approach is referred to as REIT, which is summarized in Algorithm 1. After Algorithm 1 attains $\Delta\sigma^*$, we can exploit the method in [48] to transform $\Delta\sigma^*$ into an EIT image with standard dimensions of either 22 × 32 or 32 × 32.

### C. Selection of $\eta$

With an appropriate $\sigma_n$, the $3\sigma_n$ rule has been adopted for outlier detection [49], [50]. Specifically, the samples that fall outside $3\sigma_n$ interval are likely to be outliers as 99.7% of samples fall within $3\sigma_n$ interval for normal distribution. For unimodal distributions, the probability of being within the interval is at least 95% by the Vysochanskij-Petunin inequality [51]. Therefore, the interval $[-3\sigma_n, 3\sigma_n]$ can be considered as a baseline to identify outliers, indicating that $\eta \approx 3$. In Section IV, we investigate the impact of $\eta$ on EIT performance to verify the abovementioned analysis.

### D. Convergence Analysis

In this section, the convergence behavior of the proposed REIT is analyzed in the following theorems. The first one studies the convergence of the objective values.

*Theorem 1:* Let $f(\Delta\sigma^k, o^k)$ be the objective value generated by Algorithm 1. Then, the following hold.

1) The sequence $\{f(\Delta\sigma^k, o^k)\}_{k\in\mathbb{N}}$ is nonincreasing.
2) $f(\Delta\sigma^k, o^k)$ is lower bounded.

As a result, $\{f(\Delta\sigma^k, o^k)\}_{k\in\mathbb{N}}$ is convergent.

*Proof:* See Appendix A.

We then analyze the sequence behavior in Theorem 2.

*Theorem 2:* Let $\{(\Delta\sigma^k, o^k)\}_{k\in\mathbb{N}}$ be the sequence generated by Algorithm 1. Additionally, $\{(\Delta\sigma^k, o^k)\}_{k\in\mathbb{N}}$ is considered to be bounded. Then, the following hold:

1)

$$\lim_{K_{\max}\to+\infty} \sum_{k=1}^{K_{\max}} \left(\left\|\Delta\sigma^{k+1} - \Delta\sigma^k\right\|_2^2 + \left\|o^{k+1} - o^k\right\|_2^2\right) < +\infty. \tag{16}$$

Hence, we obtain

$$\lim_{K_{\max}\to+\infty} \left(\left\|\Delta\sigma^{k+1} - \Delta\sigma^k\right\|_2 + \left\|o^{k+1} - o^k\right\|_2\right) = 0. \tag{17}$$

2) The objective function $f$ is bounded below and has the Kurdyka–Łojasiewicz (KŁ) property, and the function $(x, o) \mapsto \|\widetilde{W}(\Delta v - J\Delta\sigma - o)\|_2^2 + \lambda_1\|\widetilde{Q}\Delta\sigma\|_2^2$ has a Lipschitz gradient. Then, the sequence $\{(x^k, o^k)\}_{k\in\mathbb{N}}$ converges to a critical point of (7).
3) Algorithm 1 converges with at least a sublinear rate.

*Proof:* See Appendix B.

### E. Computational Complexity

In this section, we analyze the computational complexity of REIT. First, we denote the channel number as $N$ that is determined by the excitation measurement method, while the dimensions Jacobian matrix are $N \times M$. Generally, $M$ is larger than $N$. Then, the primary computational burden in the update of $\Delta\sigma^{k+1}$ incurs a cost of $\mathcal{O}(M^3)$. For the task of updating $o^{k+1}$, the complexity is $\mathcal{O}(N\log(N))$. As a result, the total computational complexity is $\mathcal{O}(M^3)$.

## IV. EXPERIMENTAL RESULTS

In this section, we evaluate the REIT based on numerical simulation, phantom experiment, and human experiment. All experiments are implemented using MATLAB (R2023a) on a computer with Inter[1] Core[2] i9-14900k 6.0-GHz CPU and 64-GB memory.

### A. Measurement Index

To evaluate the restoration performance, we exploit image error and image correlation coefficient (Corr), which quantify the difference and similarity, respectively, between the reconstructed EIT image and ground truth or reference

$$\text{Error} = \frac{\|R^* - R\|_1}{\|R\|_1} \tag{18a}$$

$$\text{Corr} = \frac{\sum_{i=1}^{22}\sum_{j=1}^{32}\left(R_{i,j}^* - \bar{R}^*\right)\left(R_{i,j} - \bar{R}\right)}{\|R^* - \bar{R}^*\|_F\|R - \bar{R}\|_F} \tag{18b}$$

where $R_{i,j}$ is the $(i, j)$ pixel of the EIT image, $R^*$ is the rebuilt EIT image based on the corrupted EIT boundary voltages, $R$ is the ground truth or reference, while $\bar{R}^*$ and $\bar{R}$ are the average values of all pixels in $R^*$ and $R$, respectively.

In addition, four clinical indices are employed, namely, center of ventilation (CoV) [52], global inhomogeneity (GI) [53], ventral to dorsal side ratio (VtoD) [20], and right to left lung ratio (RtoL) [20]. Specifically, CoV measures the

---

[1] Registered trademark.

[2] Trademarked.

ventilation distribution influenced by gravity or various lung diseases

$$\mathrm{CoV_R} = \frac{\sum_{i=1}^{22}\sum_{j=1}^{32}\left(Y_{i,j} \times R_{i,j}\right)}{\sum_{i=1}^{22}\sum_{j=1}^{32} R_{i,j}} \tag{19}$$

where $Y_{i,j}$ is the height of the $(i, j)$ pixel relative to the ventral side.

GI is used to classify the heterogeneity of lung ventilation, which is given by

$$\mathrm{GI_R} = \frac{\sum_{(i,j)\in \mathrm{lung}} |R_{i,j} - \mathrm{median}\left(R_{\mathrm{lung}}\right)|}{\sum_{(i,j)\in \mathrm{lung}} R_{i,j}} \tag{20}$$

where $R_{\mathrm{lung}}$ denotes all the pixels in the lung area. A high GI index implies high variation among pixel tidal impedance values.

The index VtoD characterizes the difference in ventilation between the ventral and dorsal areas

$$\mathrm{VtoD_R} = \frac{\sum_{(i,j)\in \mathrm{ventral}} R_{i,j}}{\sum_{(i,j)\in \mathrm{dorsal}} R_{i,j}} \tag{21}$$

in which the ventral area consists of all pixels in 1–16 rows and dorsal area involves 17–32 rows of the EIT image.

Similarly, RtoL characterizes the difference in ventilation between right and left lungs

$$\mathrm{RtoL_R} = \frac{\sum_{(i,j)\in \mathrm{right}} \boldsymbol{R}_{i,j}}{\sum_{(i,j)\in \mathrm{left}} \boldsymbol{R}_{i,j}} \tag{22}$$

where the right area consists of all pixels in 1–16 columns and left area involves 17–32 columns of the EIT image.

Based on the four indices, the differences between the EIT images constructed from corrupted and normal EIT boundary voltages are calculated to quantify the recovery performance. For example, $\mathrm{CoV_{err}}$ is calculated as

$$\mathrm{CoV_{err}} = |\mathrm{CoV}_R - \mathrm{CoV}_{R^*}|\,. \tag{23}$$

Similarly, $\mathrm{GI_{err}}$, $\mathrm{VtoD_{err}}$, and $\mathrm{RtoL_{err}}$ are computed using the rebuilt EIT image with the corrupted EIT boundary voltages and the reference EIT image.

Note that, for $\mathrm{CoV_{err}}$, $\mathrm{GI_{err}}$, $\mathrm{VtoD_{err}}$, and $\mathrm{RtoL_{err}}$, a smaller value indicates better imaging performance.

### *B. Parameter Investigation*

This section investigates the influence of $\eta$ on imaging performance by exploiting the synthetic data generated from an FE model that is created by the Netgen software. The FE model consists of 21 396 triangular FEs, while includes realistic thorax and lung contours segmented from a computed tomography (CT) image located between the fourth and fifth ribs of an adult male. Its 16 electrodes with 10 mm diameter are equidistantly set on the surface of the thorax according to the locations of the sternum and the spine. Besides, the conductivity of nonlung area is set to 1 S/m, while that of lung areas is set to 1 and 0.3 S/m to simulate two states of lungs, respectively (i.e., two different amounts of gas in the lungs). Furthermore, the EIT boundary voltages under the two situations are calculated by applying opposite current excitation-adjacent voltage measurement mode. As described in the commercial EIT system manual, the electrode data quality becomes poor when the electrode-skin contact impedance is greater than 300 Ω. Furthermore, the current of 1 mA at 50 kHz is used to perform EIT data collection.

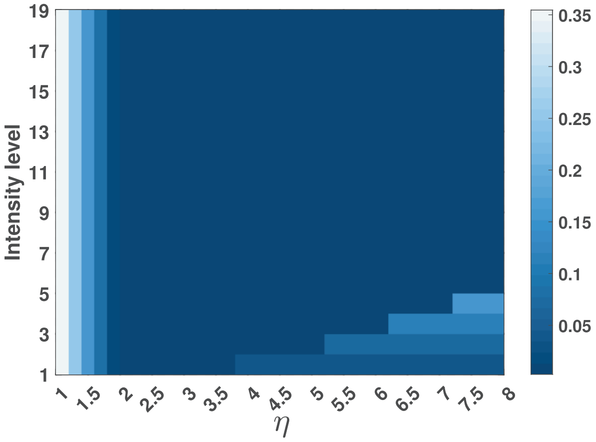

Fig. 2. EIT image errors with different intensity levels of impulsive noise and $\eta$.

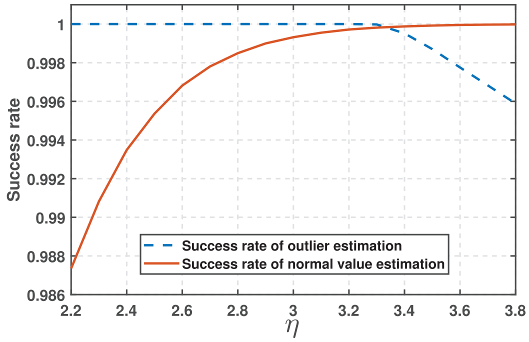

Fig. 3. Success rate versus $\eta$.

Then, the synthetic data are used to study the impact of $\eta$ on the performance with different intensities of impulsive noise. Specifically, noise is introduced to the 25th channel of the EIT boundary voltage at intensities that scale the normal entry value by factors of $1, 2, \ldots, 9, 10, 20, \ldots, 90, 100$, resulting in 19 levels in total. Subsequently, the corrupted EIT boundary voltages are exploited to reconstruct respiratory EIT images in different values of $\eta$. The results are shown in Fig. 2, where $\eta$ varies from 1 to 8 with the step size of 0.2. We see that, in low-intensity levels, the error between the EIT image based on the contaminated EIT boundary voltages and the ground truth decreases and then increases when $\eta$ increases from 1 to 8. When the intensity level is larger than 5, the EIT imaging performance improves along with the growth of $\eta$. However, if $\eta$ increases continuously, the performance will be degraded. This is because a small amplitude of impulsive noise requires a narrow confidence interval to identify, and thus, the appropriate value of $\eta$ is from 2 to 3.5. When the amplitude of impulsive noise is large, a wide confidence interval is able to distinguish the normal entries and outliers. As the confidence interval widens, it will not identify the outliers. Moreover,

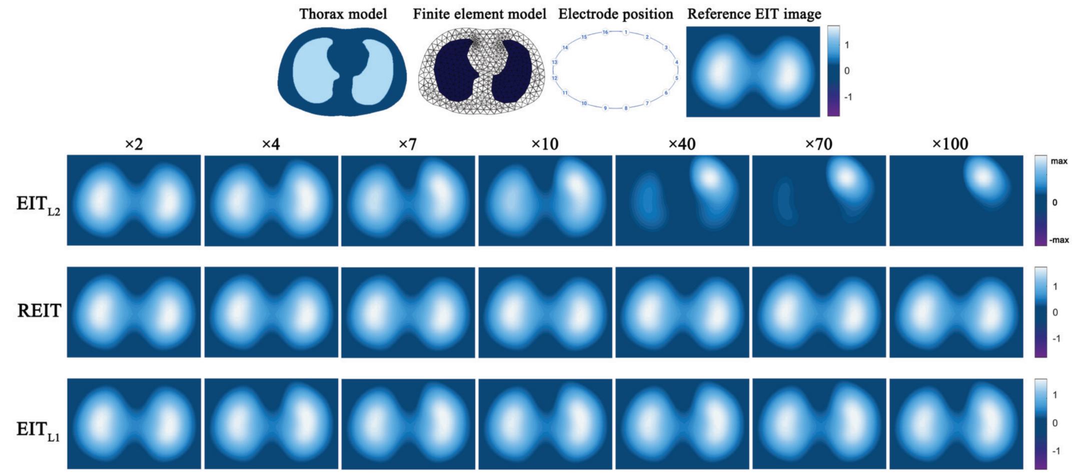

Fig. 4. Performance comparison of different methods in seven intensity levels of impulsive noise.

we validate the empirical $3\sigma_n$ rule using the synthetic data generated from the FE model, where the intensity level of impulsive noise is set to 11 in the 25th channel. We first exploit (14) to calculate the standard deviation. Then, the success rates of normal value estimation and outlier estimation are 100% when $\eta$ controlling the confidence interval varies from 2.2 to 3.8. To conduct further verification, we exploit the synthetic data with a large number of samples. Specifically, we generate a vector of 10 000 samples following the zero-mean Gaussian distribution. Then, we randomly select 10% samples and add impulsive noise to them, where the amplitudes of outliers are 100 times greater than those of the original samples. The average results with 1000 trials are plotted in Fig. 3, where $\eta$ varies from 2.2 to 3.8. It is seen that, as $\eta$ increases, the success rate of normal value estimation increases, while that of outlier estimation decreases. This is because a larger confidence interval will contain more normal values and outliers, resulting in that fewer normal points are misclassified as outliers, while more anomalies are considered as normal points. That is, the $3\sigma_n$ confident interval is able to accurately identify outliers, while misidentifies less than 0.1% of normal values.

### C. Numerical Simulation

In this section, we compare the proposed algorithm with a nonrobust method $\mathrm{EIT_{L2}}$ (GREIT) [37] and a robust approach $\mathrm{EIT_{L1}}$ [33] using the synthetic data.

Fig. 4 shows the reconstructed EIT images by different algorithms versus seven intensity levels of impulsive noise. We observe that $\mathrm{EIT_{L2}}$, $\mathrm{EIT_{L1}}$, and the suggested REIT are able to attain high-quality imaging performance in intensity level 2. When the level is larger than 2, outliers deform the left lung in EIT images generated by $\mathrm{EIT_{L2}}$ and $\mathrm{EIT_{L1}}$, while REIT obtains a high-quality EIT image. As the intensity level reaches 40, $\mathrm{EIT_{L2}}$ cannot achieve a correct EIT image, but $\mathrm{EIT_{L1}}$ and REIT can attain a satisfactory EIT image, where the image quality of REIT is higher than that of $\mathrm{EIT_{L1}}$. In addition, the errors and correlation coefficients are illustrated in Fig. 5. We see that the REIT attains the smallest errors and largest correlation coefficients in all intensity levels. The errors and correlation coefficients of $\mathrm{EIT_{L2}}$ increase and decrease, respectively, with the intensity level grows. For $\mathrm{EIT_{L1}}$, its performance degrades and then stabilizes.

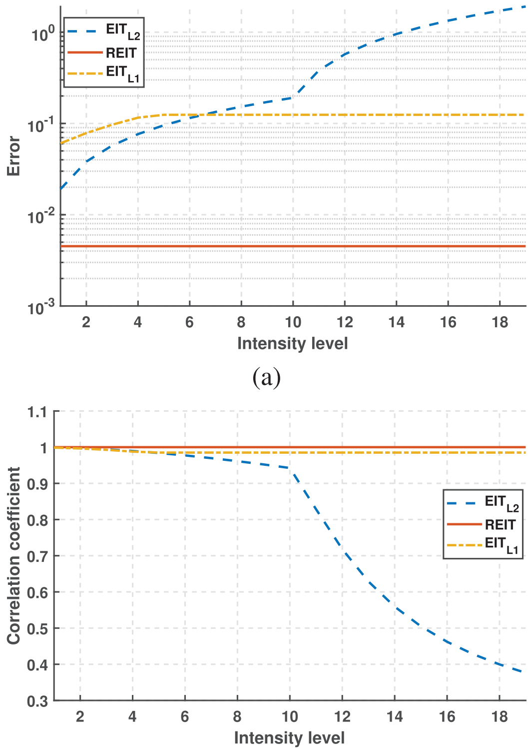

(a)

(b)

Fig. 5. Measurement indices of different methods in 19 intensity levels of impulsive noise. (a) Error versus intensity level. (b) Correlation coefficient versus intensity level.

Furthermore, the proposed algorithm is evaluated with different numbers of channels corrupted by impulsive noise. The three situations are designed to simulate realistic scenarios, in which 24, 48, and 96 channels are contaminated. They correspond to the three real-world scenarios, where the contact impedance of electrode #1 changed, electrode #1 is detached, while both electrodes #1 and #8 are detached. In these

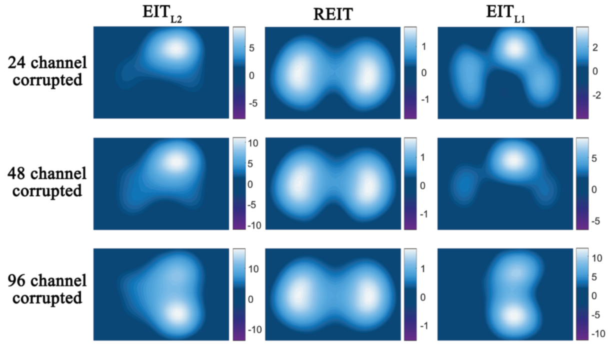

Fig. 6. Performance comparison of different methods in three outlier-contaminated channel numbers.

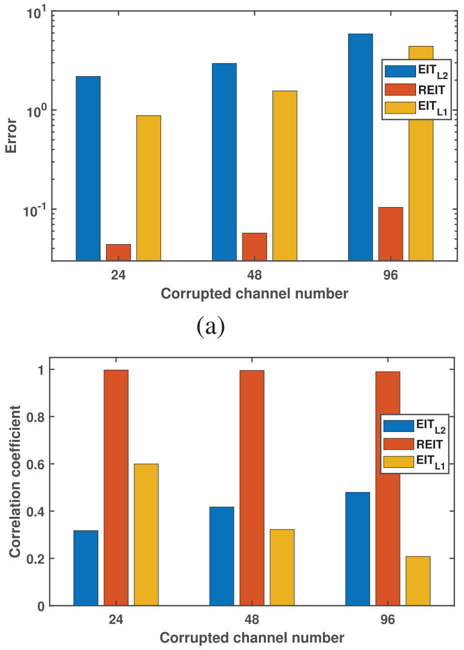

(a)

(b)

Fig. 7. Measurement indices of different methods in three outlier-contaminated channel numbers. (a) Error versus outlier-contaminated channel number. (b) Correlation coefficient versus outlier-contaminated channel number.

scenarios, the voltages of the selected channels are multiplied by 20, which models the additive impulsive noise. Electrode #1 is used to excite current and involved in excitation and measurement, while both electrode #1 and #8 are involved in excitation and measurement. The EIT images reconstructed by $EIT_{L2}$, $EIT_{L1}$, and REIT are exhibited in Fig. 6. It is seen that $EIT_{L2}$ cannot reconstruct correct EIT images in all cases. For $EIT_{L1}$, the EIT image in 24 outlier-contaminated channels presents two lungs, but the image deviates from the ground truth. When the number of the noisy channels reaches 48 and 96, its performance degrades severely. In contrast with $EIT_{L2}$ and $EIT_{L1}$, REIT attains high-quality EIT images in all situations. The corresponding indices are plotted in Fig. 7. It is observed that $EIT_{L1}$ is superior to $EIT_{L2}$ and $EIT_{L1}$ in terms of both error and correlation coefficient.

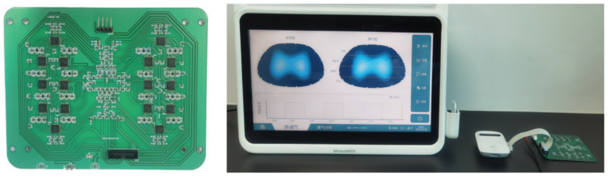

Fig. 8. Resistor phantom.

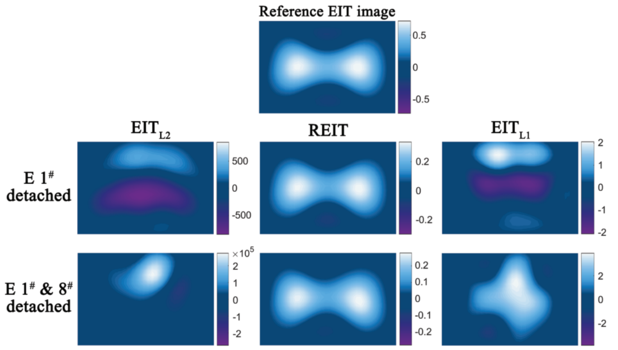

Fig. 9. Illustration of EIT images by different algorithms with detached electrodes.

TABLE I

PERFORMANCE BY DIFFERENT ALGORITHMS ON PHANTOM DATA WITH DETACHED ELECTRODES

| Method | Metric | 24 | 48 | 96 |
|---|---|---|---|---|
| $EIT_{L2}$ | Error | 2.18 | 2.95 | 5.86 |
| | Corr | 0.32 | 0.42 | 0.48 |
| REIT | Error | **0.04** | **0.06** | **0.10** |
| | Corr | **1.00** | **1.00** | **0.99** |
| $EIT_{L1}$ | Error | 0.88 | 1.56 | 4.40 |
| | Corr | 0.60 | 0.32 | 0.21 |

### *D. Phantom Experiment*

In this section, we compare the three algorithms using phantom data. Fig. 8 shows the devised resistor phantom. In detail, it consists of 136 resistors of 200 Ω with a precision of 0.01% and 24 digital potentiometers with a resistance change range from 4.68 Ω to 1.2k Ω. Controlled by a microcontroller, the 24 potentiometers are divided into two units to simulate impedance changes caused by ventilation on both sides of the lungs. Based on the breathing waveform of a healthy male, the inhalation time and exhalation time are set to 1.85 and 2.4 s, respectively. The resistor phantom is connected to the EIT system (Ventom-100, Medias Corporation, Suzhou, China) through 16 ports.

To simulate impulsive noise caused by EIT electrode detachment in clinical practice, the conduction wire of electrode #1 is cut, and then, respiratory EIT boundary voltages are collected for 1 min. Subsequently, the same procedure is carried out for electrode #8. The EIT boundary voltages without electrode detachment are exploited to reconstruct a reference EIT image that can be considered as the ground truth.

Fig. 9 shows the EIT images reconstructed by $EIT_{L2}$, $EIT_{L1}$, and REIT. It is observed that the $EIT_{L2}$ and $EIT_{L1}$ cannot rebuild effective EIT images when electrode #1 is detached, as well as when both electrodes #1 and #8 are

TABLE II
EVALUATION INDICES BY DIFFERENT ALGORITHMS ON HUMAN DATA OF SUBJECT 1

| Method | Detached | Error | Corr | $\mathrm{CoV_{err}}$ | $\mathrm{GI_{err}}$ | $\mathrm{VtoD_{err}}$ | $\mathrm{RtoL_{err}}$ |
|---|---|---|---|---|---|---|---|
| $\mathrm{EIT_{L2}}$ | #1 | 283.47 | 0.05 | 31.09 | 3.71 | 1.25 | 4.96 |
| | #1&#8 | 313912.70 | -0.35 | 66.02 | 6.94 | 1.59 | 0.08 |
| REIT | #1 | **0.29** | **0.99** | **1.21** | **0.08** | **0.13** | **0.05** |
| | #1&#8 | **0.32** | **0.96** | **1.01** | **0.21** | **0.15** | **0.06** |
| $\mathrm{EIT_{L1}}$ | #1 | 10.80 | 0.25 | 1170.02 | 272.07 | 2.06 | 1.86 |
| | #1&#8 | 40.83 | -0.14 | 7.13 | 0.74 | 0.79 | 29.88 |

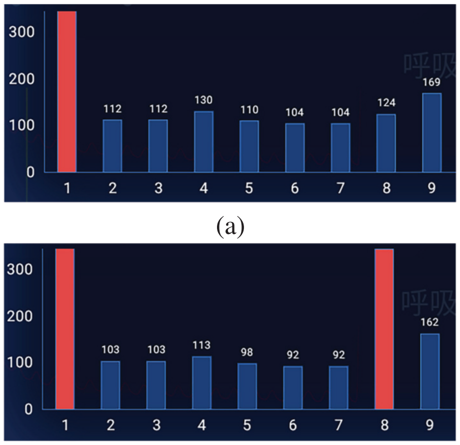

(a)

(b)

Fig. 10. Illustration of electrode contact impedance on Case 1 of human data. (a) Contact impedance with electrode #1 being affected. (b) Contact impedance with electrodes #1 and #8 being affected.

detached. By contrast, REIT reconstructs the EIT images that are comparable to the ground truth. In addition, two metrics are calculated to evaluate $\mathrm{EIT_{L2}}$, $\mathrm{EIT_{L1}}$, and REIT. The results are tabulated in Table I. It is known that REIT attains the lowest errors and highest correlation coefficients among the three approaches.

### *E. Human Experiment*

In this section, we further evaluate the proposed algorithm using the human data. The two human trials have been approved by the Ethics Committees of the Air Force Medical University (KY20224101-1) and the Human Research Ethics Committee of the Tangdu Hospital of Air Force Medical University (NO. K202212-13). Written informed consent has been obtained from all the subjects. Specifically, the EIT boundary voltages of the first subject are collected in the laboratory. A healthy male (age: 36 years old; height: 175 cm; weight: 75 kg) wears a commercial EIT electrode belt (Ventom-100, Medias Corporation, Suzhou, China) located between the fourth and fifth ribs. The subject keeps quite breathing in a standing position. After guarantee of good contact between all electrodes and skin (electrode contact impedance < 200 Ω), thoracic EIT boundary voltages are collected for 1 min. Then, a piece of paper is inserted between electrode #1 and skin for electrode detachment to generate strong interference and then thoracic EIT data are collected for 1 min. Following that, the same procedure is executed for electrode #8. Thoracic EIT boundary voltages are collected for 1 min to ensure that the corrupted data are obtained. In addition, 1 min enables us to observe the stable periodic variations of the signal. Fig. 10 illustrates the electrode contact impedance when electrode #1 is affected, while both electrodes #1 and #8 are influenced. We see that the contact impedance of well-contacted electrodes is less than 200 Ω, while that of affected electrodes is larger than 300 Ω.

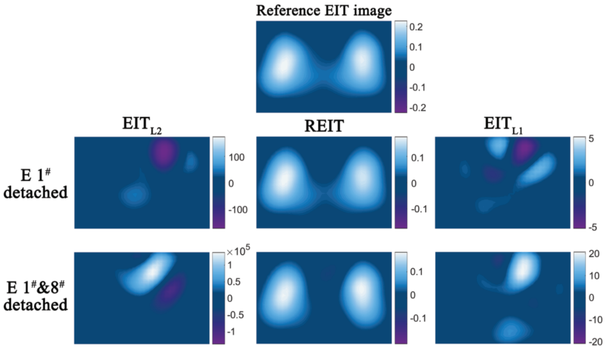

Fig. 11. Illustration of EIT images reconstructed by different methods on human data of Subject 1.

TABLE III
RUNTIME COMPARISON OF DIFFERENT METHODS ON HUMAN DATA OF SUBJECT 1

| Method | $\mathrm{EIT_{L2}}$ | REIT | $\mathrm{EIT_{L1}}$ |
|---|---|---|---|
| Time (s) | **0.015** | 0.155 | 0.715 |

Similar to the phantom experiment, the image metrics and EIT clinical indices of tidal EIT images are exploited to evaluate the performance of the proposed algorithm. The reconstructed EIT images by different methods on Subject 1 are shown in Fig. 11. It is apparent that the rebuilt EIT image by REIT is almost the same to the reference EIT image, while $\mathrm{EIT_{L2}}$ and $\mathrm{EIT_{L1}}$ cannot reconstruct correct EIT image with electrode #1 being affected. When electrodes #1 and #8 are influenced, REIT still rebuilds a satisfactory EIT image that is much better than the EIT images reconstructed by the competing algorithms. In addition, the six measurement indices are tabulated in Table II. We see that the proposed REIT has an absolute advantage in image quality indices and clinical indices. Furthermore, we compare the runtime of different methods in Table III. It is observed that the proposed method is much faster than $\mathrm{EIT_{L1}}$ but lower than $\mathrm{EIT_{L2}}$. As our algorithm requires dozens of iterations, it may not allow real-time monitoring. However, its efficiency can be improved using several techniques. Note that updating

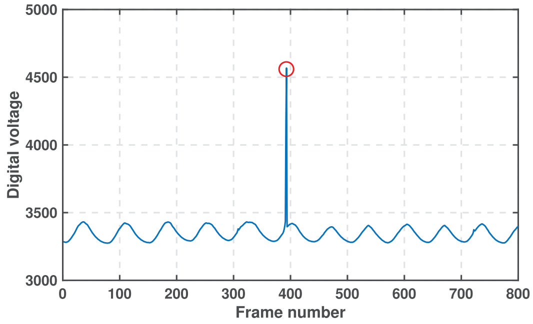

Fig. 12. EIT digital voltage calculated as the sum of absolute values of 192 channels.

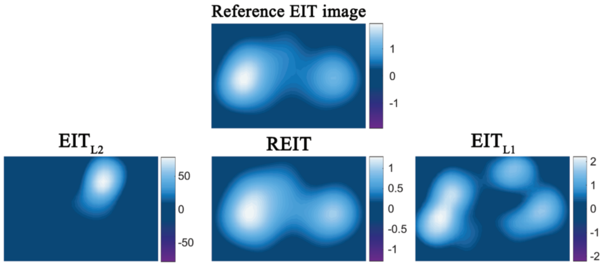

Fig. 13. Illustration of EIT images reconstructed by different methods on human data of Subject 2.

$\Delta\sigma$ requires computing the inverse of a matrix, leading to high computational complexity. Therefore, we can employ the steepest gradient descent method to replace the current scheme, which is able to decrease the runtime. In addition, for iterative multivariable optimization, optimizing one variable while fixing remaining variables is not so beneficial. This is because a perfect optimization of one part might be rendered obsolete when the other part is altered. Thereby, we can substitute gradient descent for the steepest gradient descent method and then tune the corresponding step-size to decrease the iteration number, further reducing the running time. On the other hand, $o$ is updated in scalar form, and thus, parallel computing can be employed to decrease runtime.

For Subject 2, the clinical EIT data are acquired from a patient suffering from left pulmonary nodule, who is scheduled for laparoscopic lung parenchymal resection in the Department of Thoracic Surgery of Tangdu Hospital, Air Force Medical University, Xi'an, China. The EIT boundary voltages are collected preoperatively in the right lateral position with a commercial EIT system (VenTom-100). During data collection, the patient keeps spontaneous breathing, whereas deliberate movement, medical treatment, and nursing are not restricted. Therefore, the EIT boundary voltages are inevitably corrupted, and Fig. 12 plots the sum of digital voltages of 192 channels, where the 391st, 392nd, and 393rd frames are corrupted by impulsive noise. We select the 393rd frame with the strongest interference to reconstruct an EIT image for evaluating the proposed REIT.

The EIT images rebuilt by different algorithms are plotted in Fig. 13. It is seen that the imaging performance of EIT$_{\mathrm{L2}}$ is the worst, such that two lungs cannot be discovered. In the EIT image by EIT$_{\mathrm{L1}}$, only the right lung can be identified although its shape is changed. By contrast with EIT$_{\mathrm{L2}}$ and EIT$_{\mathrm{L1}}$, REIT obtains a higher quality EIT image that exhibits the real situation of the patient. Besides, Table IV lists six indices, viz. error, Corr, CoV$_{\mathrm{err}}$, GI$_{\mathrm{err}}$, VtoD$_{\mathrm{err}}$, and RtoL$_{\mathrm{err}}$. It is seen that REIT demonstrates superiority over EIT$_{\mathrm{L2}}$ and EIT$_{\mathrm{L1}}$ in all image quality indices and clinical indices.

TABLE IV

Evaluation Indices by Different Algorithms on Human Data of Subject 2

| Method | Error | Corr | CoV$_{\mathrm{err}}$ | GI$_{\mathrm{err}}$ | VtoD$_{\mathrm{err}}$ | RtoL$_{\mathrm{err}}$ |
|---|---|---|---|---|---|---|
| EIT$_{\mathrm{L2}}$ | 16.59 | 0.07 | 15.10 | 0.50 | 0.95 | 546.95 |
| REIT | **0.23** | **0.96** | **0.98** | **0.01** | 0.15 | **0.04** |
| EIT$_{\mathrm{L1}}$ | 0.57 | 0.83 | 2.42 | 0.03 | **0.10** | 0.19 |

## V. CONCLUSION

In this article, we reformulated the boundary voltage change model for thoracic EIT imaging, where the noise is divided into dense Gaussian and sparse outlier components. We then established the optimization problem using $\ell_2$-norm and $\ell_0$-norm, where the former and the latter are exploited to handle the Gaussian noise and the outliers, respectively. Besides, we adopted proximal AM and PGD to tackle the resultant optimization task. Although the proposed REIT introduced a penalty parameter related to the $\ell_0$-norm, we provided an adaptive strategy for its determination. Specifically, it can be considered as a threshold to differentiate the normal and faulty channels. We also analyzed convergence behavior of REIT. Specifically, we proved that the objective value sequence is convergent, while the variable sequence converges to a critical point. Experimental results based on synthetic, phantom, and human data demonstrated that REIT achieves higher quality EIT images than conventional algorithms in the presence of impulsive noise.

As our algorithm requires dozens of iterations, it may not allow real-time monitoring. Hence, one future research direction is to decrease the computational complexity to reduce the processing time within 0.05 s. Besides, we will consider the boundary shape mismatch problem to enhance the robustness of our algorithm against this factor.

## APPENDIX A
## PROOF OF THEOREM 1

*Property 1):* As (9) attains the optimal solution to (8a), we obtain the following inequality:

$$\begin{aligned}&\left\|\widetilde{W}\left(\Delta v - J\Delta\sigma^{k+1} - o^{k}\right)\right\|_2^2 + \lambda_1\left\|\widetilde{Q}\Delta\sigma^{k+1}\right\|_2^2\\ &\quad + \mu\left\|\Delta\sigma^{k+1} - \Delta\sigma^{k}\right\|_2^2\\ &\le \left\|\widetilde{W}\left(\Delta v - J\Delta\sigma^{k} - o^{k}\right)\right\|_2^2 + \lambda_1\left\|\widetilde{Q}\Delta\sigma^{k}\right\|_2^2 \qquad (24a)\\ &\Leftrightarrow f\left(\Delta\sigma^{k+1}, o^{k}\right) - f\left(\Delta\sigma^{k}, o^{k}\right) \le -\mu\left\|\Delta\sigma^{k+1} - \Delta\sigma^{k}\right\|_2^2. \qquad (24b)\end{aligned}$$

On the other hand, since (12) seeks an optimal solution of (8b), we have

$$\begin{aligned}&\left\|\widetilde{W}\left(\Delta v - J\Delta\sigma^{k+1} - o^{k+1}\right)\right\|_2^2 + \lambda_2\left\|o^{k+1}\right\|_0 + \mu\left\|o^{k+1} - o^{k}\right\|_2^2\\ &\le \left\|\widetilde{W}\left(\Delta v - J\Delta\sigma^{k} - o^{k}\right)\right\|_2^2 + \lambda_2\left\|o^{k}\right\|_0 \qquad (25a)\end{aligned}$$

$$\Leftrightarrow f\left(\Delta\sigma^{k+1}, o^{k+1}\right) - f\left(\Delta\sigma^{k+1}, o^{k}\right) \le -\mu \left\| o^{k+1} - o^{k} \right\|_2^2 . \quad (25b)$$

Combining (24b) and (25b) results in

$$\begin{aligned} & f\left(\Delta\sigma^{k+1}, o^{k+1}\right) - f\left(\Delta\sigma^{k}, o^{k}\right) \\ & \le -\mu \left( \left\| \Delta\sigma^{k+1} - \Delta\sigma^{k} \right\|_2^2 + \left\| o^{k+1} - o^{k} \right\|_2^2 \right) \\ & \le 0 \end{aligned} \quad (26)$$

which indicates that $f(\Delta\sigma^k, o^k)$ is nonincreasing after updating the variables. The proof is complete. ■

*Property 2):* Since $f(\Delta\sigma, o)$ is comprised of three terms based on $\ell_2$-norm and $\ell_0$-norm, respectively, $f(\Delta\sigma^k, o^k) \ge 0$ must hold.

As a result, based on Properties 1) and 2), the convergence of $\{f(\Delta\sigma^k, o^k)\}_{k\in\mathbb{N}}$ is guaranteed. The proof is complete. ■

## APPENDIX B
## PROOF OF THEOREM 2

*Property 1):* We re-express (26) as

$$\begin{aligned} & \left\| \Delta\sigma^{k+1} - \Delta\sigma^{k} \right\|_2^2 + \left\| o^{k+1} - o^{k} \right\|_2^2 \\ & \quad \le \frac{f\left(\Delta\sigma^{k}, o^{k}\right) - f\left(\Delta\sigma^{k+1}, o^{k+1}\right)}{\mu} . \end{aligned} \quad (27)$$

By induction on $k$, we obtain

$$\begin{aligned} & \lim_{K_{\max}\to+\infty} \sum_{k=1}^{K_{\max}} \left( \left\| \Delta\sigma^{k+1} - \Delta\sigma^{k} \right\|_2^2 + \left\| o^{k+1} - o^{k} \right\|_2^2 \right) \\ & \quad \le \lim_{K_{\max}\to+\infty} \frac{f\left(\Delta\sigma^{1}, n^{1}\right) - f\left(\Delta\sigma^{K_{\max}+1}, n^{K_{\max}+1}\right)}{\mu} \\ & \quad < +\infty . \end{aligned} \quad (28)$$

Therefore, we have

$$\lim_{K_{\max}\to+\infty} \left( \left\| \Delta\sigma^{K_{\max}+1} - \Delta\sigma^{K_{\max}} \right\|_2^2 + \left\| o^{K_{\max}+1} - o^{K_{\max}} \right\|_2^2 \right) = 0. \quad (29)$$

The proof is complete. ■

*Property 2):* It is apparent that $f$ is bounded as follows. In addition, as the $\ell_0$-norm is semi-algebraic, it is definable in an o-minimal structure [54]. We conclude that $f$ has the Kproperty.

Then, we prove that $(x, o) \mapsto \|\widetilde{W}(\Delta v - J\Delta\sigma - o)\|_2^2 + \lambda_1 \|\widetilde{Q}\Delta\sigma\|_2^2$ has a Lipschitz gradient. Its second derivative with respect to $\Delta\sigma$ is

$$\begin{aligned} & \left\| \frac{\partial^2 \left\| \widetilde{W}\left(\Delta v - J\Delta\sigma - o\right) \right\|_2^2 + \lambda_1 \left\| \widetilde{Q}\Delta\sigma \right\|_2^2}{\partial^2 \Delta\sigma} \right\|_2 && (30a) \\ & = \left\| 2J^{\mathrm{T}}\widetilde{W}^{\mathrm{T}}\widetilde{W}J + 2\lambda_1 \widetilde{Q}^{\mathrm{T}}\widetilde{Q} \right\|_2 && (30b) \\ & \le 2\left\| J^{\mathrm{T}} W J \right\|_2 + 2\lambda_1 \left\| Q \right\|_2 && (30c) \\ & \le 2\sigma_n^2 \left\| J \right\|_2^2 + 2\lambda_1 \left\| Q \right\|_2 && (30d) \\ & \le 2\sigma_n^2 \left\| J \right\|_F^2 + 2\lambda_1 \left\| Q \right\|_F . && (30e) \end{aligned}$$

When $\|J\|_F$ and $\|Q\|_F$ are finite, we attain

$$\left\| \frac{\partial^2 \left\| \widetilde{W}\left(\Delta v - J\Delta\sigma - o\right) \right\|_2^2 + \lambda_1 \left\| \widetilde{Q}\Delta\sigma \right\|_2^2}{\partial^2 \Delta\sigma} \right\|_2 < +\infty . \quad (31)$$

Thereby, the function $(x, o) \mapsto \left\| \widetilde{W}(\Delta v - J\Delta\sigma - o) \right\|_2^2 + \lambda_1 \left\| \widetilde{Q}\Delta\sigma \right\|_2^2$ has a Lipschitz gradient with respect to $\Delta\sigma$.

We then prove that it has a Lipschitz gradient with respect to $o$

$$\left\| \frac{\partial^2 \left\| \widetilde{W}\left(\Delta v - J\Delta\sigma - o\right) \right\|_2^2}{\partial^2 o} \right\|_2 = \|2W\|_2 \le 2\sigma_n^2, \ \forall o \in \mathbb{R}^M . \quad (32)$$

As a result, the function $\left\| \widetilde{W}(\Delta v - J\Delta\sigma - o) \right\|_2^2 + \lambda_1 \left\| \widetilde{Q}\Delta\sigma \right\|_2^2$ has a Lipschitz gradient.

Furthermore, as $\min_{\Delta\sigma, o} f(\Delta\sigma, o)$ is solved using PAM and $(\Delta\sigma^k, o^k)_{k\in\mathbb{N}}$ is bounded, $\{(\Delta\sigma^k, o^k)\}_{k\in\mathbb{N}}$ converges to a critical point of (7) based on [55, Theorem 6.2]. The proof is complete. ■

*Property 3):* As $f$ has the Kproperty, based on Theorem 1 in [54], our method converges at least sublinearly. The proof is complete. ■

## REFERENCES

[1] M. Cheney, D. Isaacson, and J. C. Newell, "Electrical impedance tomography," *SIAM Rev.*, vol. 41, no. 1, pp. 85–101, 1999.

[2] Z. Chen, J. Xiang, P.-O. Bagnaninchi, and Y. Yang, "MMV-net: A multiple measurement vector network for multifrequency electrical impedance tomography," *IEEE Trans. Neural Netw. Learn. Syst.*, vol. 34, no. 11, pp. 8938–8949, Nov. 2022.

[3] I. Frerichs et al., "Chest electrical impedance tomography examination, data analysis, terminology, clinical use and recommendations: Consensus statement of the translational EIT developmeNt stuDy group," *Thorax*, vol. 72, no. 1, pp. 83–93, Jan. 2017.

[4] Z. Liu, H. Gu, Z. Chen, P. Bagnaninchi, and Y. Yang, "Dual-modal image reconstruction for electrical impedance tomography with overlapping group lasso and Laplacian regularization," *IEEE Trans. Biomed. Eng.*, vol. 70, no. 8, pp. 2362–2373, Aug. 2023.

[5] Z. Zhao, F. Fu, and I. Frerichs, "Thoracic electrical impedance tomography in Chinese hospitals: A review of clinical research and daily applications," *Physiological Meas.*, vol. 41, no. 4, Apr. 2020, Art. no. 04TR01.

[6] M. I. Page, R. Nicholson, M. H. Tawhai, A. R. Clark, and H. Kumar, "Improved electrical impedance tomography reconstruction via a Bayesian approach with an anatomical statistical shape model," *IEEE Trans. Biomed. Eng.*, vol. 70, no. 8, pp. 2486–2495, Aug. 2023.

[7] D. W. Kaczka, "Imaging the lung in ARDS: A primer," *Respiratory Care*, vol. 69, no. 8, pp. 1011–1024, Aug. 2024.

[8] M. Soleimani, O. Dorn, and W. R. B. Lionheart, "A narrow-band level set method applied to EIT in brain for cryosurgery monitoring," *IEEE Trans. Biomed. Eng.*, vol. 53, no. 11, pp. 2257–2264, Nov. 2006.

[9] Z. R. Gatabi, M. Mirhoseini, N. Khajeali, I. R. Gatabi, M. Dabbaghianamiri, and S. Dorri, "The accuracy of electrical impedance tomography for breast cancer detection: A systematic review and meta-analysis," *Breast J.*, vol. 2022, May 2022, Art. no. 8565490.

[10] S. K. Konki, A. K. Khambampati, and K. Y. Kim, "Fetal imaging with dynamic electrical impedance tomography technique," *J. Med. Imag. Health Informat.*, vol. 9, no. 1, pp. 23–31, Jan. 2019.

[11] M. Mosing, J. M. Cheong, B. Müller, S. H. Böhm, G. Hosgood, and A. Raisis, "Determination of tidal volume by electrical impedance tomography (EIT) after indirect two-point calibration," *Physiological Meas.*, vol. 43, no. 3, Mar. 2022, Art. no. 035005.

[12] A. H. Jonkman et al., "Lung recruitment assessed by electrical impedance tomography (RECRUIT): A multicenter study of COVID-19 acute respiratory distress syndrome," *Amer. J. Respiratory Crit. Care Med.*, vol. 208, no. 1, pp. 25–38, Jul. 2023.

[13] J. Kobylianskii, A. Murray, D. Brace, E. Goligher, and E. Fan, "Electrical impedance tomography in adult patients undergoing mechanical ventilation: A systematic review," *J. Crit. Care*, vol. 35, pp. 33–50, Oct. 2016.

[14] R. Arriagada, M. C. Bachmann, C. San Martin, M. Rauseo, and D. Battaglini, "Electrical impedance tomography: Usefulness for respiratory physiotherapy in critical illnesses," *Medicina Intensiva*, vol. 48, no. 7, pp. 403–410, 2024.

[15] E. Spinelli et al., "Electrical impedance tomography in perioperative medicine: Careful respiratory monitoring for tailored interventions," *BMC Anesthesiol.*, vol. 19, no. 1, pp. 1–11, Dec. 2019.

[16] L. Yang et al., "Electrical impedance tomography as a bedside assessment tool for COPD treatment during hospitalization," *Frontiers Physiol.*, vol. 15, Mar. 2024, Art. no. 1352391.

[17] I. Frerichs and Z. Zhao, "Electrical impedance tomography for chest imaging in acute respiratory failure," *Eur. Respiratory J.*, vol. 54, no. 4, Oct. 2019, Art. no. 1901497.

[18] C. Dimas, N. Uzunoglu, and P. P. Sotiriadis, "An efficient point-matching method-of-moments for 2D and 3D electrical impedance tomography using radial basis functions," *IEEE Trans. Biomed. Eng.*, vol. 69, no. 2, pp. 783–794, Feb. 2022.

[19] I. Frerichs, S. Pulletz, G. Elke, B. Gawelczyk, A. Frerichs, and N. Weiler, "Patient examinations using electrical impedance tomography—Sources of interference in the intensive care unit," *Physiological Meas.*, vol. 32, no. 12, pp. L1–L10, Dec. 2011.

[20] Z. Xiao et al., "Regional ventilation distribution before and after laparoscopic lung parenchymal resection," *Physiological Meas.*, vol. 45, no. 1, Jan. 2024, Art. no. 015004.

[21] L. Yang et al., "Visualizing pursed lips breathing of patients with chronic obstructive pulmonary disease through evaluation of global and regional ventilation using electrical impedance tomography," *Physiological Meas.*, vol. 45, no. 4, Apr. 2024, Art. no. 045005.

[22] Y. Asfaw and A. Adler, "Automatic detection of detached and erroneous electrodes in electrical impedance tomography," *Physiological Meas.*, vol. 26, no. 2, pp. S175–S183, Apr. 2005.

[23] A. Adler, "Accounting for erroneous electrode data in electrical impedance tomography," *Physiological Meas.*, vol. 25, no. 1, pp. 227–238, Feb. 2004.

[24] A. E. Hartinger, R. Guardo, A. Adler, and H. Gagnon, "Real-time management of faulty electrodes in electrical impedance tomography," *IEEE Trans. Biomed. Eng.*, vol. 56, no. 2, pp. 369–377, Feb. 2009.

[25] L. Yang et al., "Removing clinical motion artifacts during ventilation monitoring with electrical impedance tomography: Introduction of methodology and validation with simulation and patient data," *Frontiers Med.*, vol. 9, Jan. 2022, Art. no. 817590.

[26] Y. Shi, K. Yang, M. Wang, H. Su, B. Yang, and F. Fu, "Inadequate data augmentation with convolutional neural network in brain electrical impedance tomography," *IEEE Sensors J.*, vol. 24, no. 13, pp. 21490–21499, Jul. 2024.

[27] Y. Shi, Y. Lou, M. Wang, K. Yang, Z. Gao, and F. Fu, "Densely connected convolutional neural network-based invalid data compensation for brain electrical impedance tomography," *IEEE Trans. Comput. Imag.*, vol. 10, pp. 143–153, 2024.

[28] Y. Shi et al., "A fully connected neural network-based voltage compensation method for accurate reconstruction in brain electrical impedance tomography," *Biomed. Signal Process. Control*, vol. 86, Sep. 2023, Art. no. 105252.

[29] W. Herzberg, A. Hauptmann, and S. J. Hamilton, "Domain independent post-processing with graph U-nets: Applications to electrical impedance tomographic imaging," *Physiological Meas.*, vol. 44, no. 12, Dec. 2023, Art. no. 125008.

[30] J. Ye et al., "Removal of vibration interference artifacts in electrical impedance tomography monitoring using residual learning strategy," *IEEE Trans. Instrum. Meas.*, vol. 73, pp. 1–10, 2024.

[31] K. Mason, F. Maurino-Alperovich, D. Holder, and K. Aristovich, "Noise-based correction for electrical impedance tomography," *Physiological Meas.*, vol. 45, no. 6, Jun. 2024, Art. no. 065002.

[32] T. Dai, C. Gómez-Laberge, and A. Adler, "Reconstruction of conductivity changes and electrode movements based on EIT temporal sequences," *Physiological Meas.*, vol. 29, no. 6, pp. S77–S88, Jun. 2008.

[33] A. Borsic and A. Adler, "A primal-dual interior-point framework for using the L1 or L2 norm on the data and regularization terms of inverse problems," *Inverse Problems*, vol. 28, no. 9, Sep. 2012, Art. no. 095011.

[34] H. Attouch, J. Bolte, P. Redont, and A. Soubeyran, "Proximal alternating minimization and projection methods for nonconvex problems: An approach based on the Kurdyka–Łojasiewicz inequality," *Math. Oper. Res.*, vol. 35, no. 2, pp. 438–457, May 2010.

[35] F. Wen, R. Ying, P. Liu, and T.-K. Truong, "Nonconvex regularized robust PCA using the proximal block coordinate descent algorithm," *IEEE Trans. Signal Process.*, vol. 67, no. 20, pp. 5402–5416, Oct. 2019.

[36] T. Blumensath and M. E. Davies, "Iterative thresholding for sparse approximations," *J. Fourier Anal. Appl.*, vol. 14, nos. 5–6, pp. 629–654, Dec. 2008.

[37] B. Grychtol, B. Müller, and A. Adler, "3D EIT image reconstruction with GREIT," *Physiological Meas.*, vol. 37, no. 6, pp. 785–800, May 2016.

[38] X. P. Li and H. C. So, "Robust low-rank tensor completion based on tensor ring rank via $\ell_{p,\epsilon}$-norm," *IEEE Trans. Signal Process.*, vol. 69, pp. 3685–3698, 2021.

[39] X. P. Li, Z. Liu, Z.-L. Shi, and H. C. So, "MUSIC with capped Frobenius norm: Efficient robust direction-of-arrival estimator," *IEEE Trans. Aerosp. Electron. Syst.*, vol. 59, no. 6, pp. 8090–8103, Dec. 2023.

[40] J. Nocedal and S. J. Wright, *Numerical Optimization*. Cham, Switzerland: Springer, 1999.

[41] X. P. Li, Z.-L. Shi, C.-S. Leung, and H. C. So, "Sparse index tracking with K-sparsity or E-deviation constraint via l0-norm minimization," *IEEE Trans. Neural Netw. Learn. Syst.*, vol. 34, no. 12, pp. 10930–10943, Dec. 2023.

[42] X. P. Li, Q. Liu, and H. C. So, "Rank-one matrix approximation with lp-norm for image inpainting," *IEEE Signal Process. Lett.*, vol. 27, pp. 680–684, 2020.

[43] X. P. Li, Z.-L. Shi, Q. Liu, and H. C. So, "Fast robust matrix completion via entry-wise $\ell_0$ -Norm minimization," *IEEE Trans. Cybern.*, vol. 53, no. 11, pp. 7199–7212, Nov. 2023.

[44] X.-P. Li, Z.-L. Shi, L. Huang, A. M.-C. So, and H. C. So, "ROCS: Robust one-bit compressed sensing with application to direction of arrival," *IEEE Trans. Signal Process.*, vol. 72, pp. 2407–2420, 2024.

[45] A. M. Zoubir, V. Koivunen, E. Ollila, and M. Muma, *Robust Statistics for Signal Processing*. Cambridge, U.K.: Cambridge Univ. Press, 2018.

[46] X. P. Li, Z.-Y. Wang, Z.-L. Shi, H. C. So, and N. D. Sidiropoulos, "Robust tensor completion via capped Frobenius norm," *IEEE Trans. Neural Netw. Learn. Syst.*, vol. 35, no. 7, pp. 9700–9712, Jul. 2024.

[47] D. E. Tyler, *Robust Statistics: Theory and Methods*. New York, NY, USA: Taylor & Francis, 2008.

[48] L. Yang et al., "Regional ventilation distribution in healthy lungs: Can reference values be established for electrical impedance tomography parameters?," *Ann. Transl. Med.*, vol. 9, no. 9, p. 789, May 2021.

[49] B. Xiong and Z. Yin, "A universal denoising framework with a new impulse detector and nonlocal means," *IEEE Trans. Image Process.*, vol. 21, no. 4, pp. 1663–1675, Apr. 2012.

[50] V. Jakhetiya, K. Gu, T. Singhal, S. C. Guntuku, Z. Xia, and W. Lin, "A highly efficient blind image quality assessment metric of 3-D synthesized images using outlier detection," *IEEE Trans. Ind. Informat.*, vol. 15, no. 7, pp. 4120–4128, Jul. 2019.

[51] D. Vysochanskij and Y. I. Petunin, "Justification of the 3$\sigma$ rule for unimodal distributions," *Theory Probab. Math. Statist.*, vol. 21, nos. 25–36, 1980.

[52] I. Frerichs, G. Hahn, W. Golisch, M. Kurpitz, H. Burchardi, and G. Hellige, "Monitoring perioperative changes in distribution of pulmonary ventilation by functional electrical impedance tomography," *Acta Anaesthesiologica Scandinavica*, vol. 42, no. 6, pp. 721–726, Dec. 1998.

[53] Z. Zhao, D. Steinmann, I. Frerichs, J. Guttmann, and K. Möller, "PEEP titration guided by ventilation homogeneity: A feasibility study using electrical impedance tomography," *Crit. Care*, vol. 14, no. 1, pp. 1–8, Jan. 2010.

[54] J. Bolte, S. Sabach, and M. Teboulle, "Proximal alternating linearized minimization for nonconvex and nonsmooth problems," *Math. Program.*, vol. 146, pp. 459–494, Aug. 2014.

[55] H. Attouch, J. Bolte, and B. F. Svaiter, "Convergence of descent methods for semi-algebraic and tame problems: Proximal algorithms, forward–backward splitting, and regularized Gauss–Seidel methods," *Math. Program.*, vol. 137, nos. 1–2, pp. 91–129, Feb. 2013.